RAA 2021 Vol. **21** No. **11**, 284(12pp) doi: 10.1088/1674-4527/21/11/284

http://www.raa-journal.org *http://iopscience.iop.org/raa*

Research in Astronomy and Astrophysics

Observational results of MUSER during 2014–2019

Ming-Hui Zhang (张茗惠)[1,2], Yin Zhang (张印)[1], Yi-Hua Yan (颜毅华)[1,2], Wei Wang (王威)[1], Lin-Jie Chen (陈林杰)[1], Cheng-Ming Tan (谭程明)[1,2], Su-Li Ma (马素丽)[1], Jing Huang (黄静)[1], Xing-Yao Chen (陈星瑶)[1], Bao-Lin Tan (谭宝林)[1,2], Zhichao Zhou (周志超)[1,2], Fei Liu (刘飞)[1], Li-Hong Geng (耿立红)[1], Sha Li (李沙)[1], Jing Du (杜静)[1], Cang Su (苏仓)[1], Zhi-Jun Chen (陈志军)[1] and Jun Cheng (程俊)[1]

[1] Key Laboratory of Solar Activity, National Astronomical Observatories, Chinese Academy of Sciences, Beijing 100101, China; *yyh@nao.cas.cn*

[2] School of Astronomy and Space Science, University of Chinese Academy of Sciences, Beijing 100049, China

Received 2021 February 26; accepted 2021 August 20

Abstract The solar radio signal that can be received by the ground-based telescopes covers a wide frequency range, allowing us to monitor the complex physical processes occurred from the solar surface to the vast interplanetary space. MingantU SpEctral Radioheliograph (MUSER), as the latest generation of solar dedicated radio spectral-imaging instrument in the centimeter-decimeter wavelengths, has accumulated a large number of observational data since its commissioning observation in 2014. This paper presents the main observational results identified by MUSER from 2014 to 2019, including the quiet Sun and 94 solar radio burst events. We find that there are 81 events accompanied with *Geostationary Operational Environmental Satellites* (*GOES*) soft X-ray (SXR) flares, among which the smallest flare class is B1.0. There are 13 events without accompanying any recorded flares, among which the smallest SXR intensity during the radio burst period is equivalent to level-A. The main characteristics of all radio burst events are presented, which shows the powerful ability of MUSER to capture the valuable information of the solar non-thermal processes and the importance for space weather. This work also provides a database for further in-depth research.

Key words: Sun: radio radiation — Sun: activity — Sun: flares — methods: observational

1 INTRODUCTION

Solar radio burst is the phenomenon that the intensity of radio radiation on the Sun suddenly increase due to the disturbance of eruptive activities, such as flares, filament eruptions and coronal mass ejections (CMEs). It was first discovered by radar equipments at meter wavelengths in 1942 during World War II (Hey 1946). The following studies demonstrated that the wavelength of solar radio bursts had a wide range from millimeter to ten kilometers (Dulk 1985). Recently, Solar Broadband Radio Dynamic Spectrometer of China (SBRS, 0.7–1.5, 1.0–2.0, 2.6–3.8, 4.5–7.5 and 5.2–7.6 GHz) (Fu et al. 2004b) and Ondřejov Radio Spectrograph (ORSC, 0.8–4.5 GHz) (Jiricka et al. 1993) have discovered an abundance of radio fine structures (FSs) which overlaid on the continuum emission. Based on the long-term accumulated observational data, Isliker & Benz (1994); Jiřička et al. (2001); Fu et al. (2004a) classified the FSs of radio bursts in centimeter wavelengths according to their morphology in dynamic spectra, such as type III bursts (e.g., Reid & Ratcliffe 2014), quasi-periodic pulsations (QPPs) (e.g., Tan et al. 2007, 2010), slowly drifting bursts (e.g., Maxwell & Thompson 1962), diffuse continua (e.g., Bouratzis et al. 2015), isolated broadband pulses (e.g., Bouratzis et al. 2009), spikes (e.g., Staehli & Magun 1986), laces (e.g., Karlický et al. 2001), zebra patterns (e.g., Chernov 2010), fibers (e.g., Chernov 2010) and several unusual types of radio FSs (e.g., Ning et al. 2000; Altyntsev et al. 2003; Huang et al. 2007).

These FSs which have different spectral and temporal properties and distribute at different wavelengths are related to different mechanisms (Bastian et al. 1998), including gyro-synchrotron radiation, plasma radiation and other emissions. Studying FSs is a key to understanding plasma processes in the corona. The magnetic field, density and temperature of the radio radiation source area can be deduced from the information obtained by FSs on the spectrum, such as the bandwidth, frequency and polarization (e.g., the analysis of QPPs by Tan et al. 2010, spike bursts by Huang & Nakajima 2005; Tan 2013 and lace bursts by Karlický et al. 2001). More information about the FSs can be found in the review written by Chernov (2011). However, these studies of FSs rarely involve radio imaging due to instrument limitations.

Recently, thanks to the development of observing techniques, Chen et al. (2013) researched the imaging observational data on the type III bursts over a broad frequency band at decimeter wavelengths by using the upgraded Very Large Array (VLA, 1-2 GHz frequency band for solar observations). They provided direct observational evidence for the fragmentation of energy release during the magnetic reconnection process and the correlation between hard X-ray and type III burst proposed by Aschwanden et al. (1995) et al. Similarly, Chen et al. (2015) and Yu & Chen (2019) analyzed the imaging data of VLA and found evidence of the termination shock acceleration particles and magnetohydrodynamics waves propagating in the reconnected magnetic tube. Based on the observations of Expanded Owens Valley Solar Array (EOVSA, 1–18 GHz) (Nita et al. 2016), a long-duration limb flare event on 2017 September 10 (Gary et al. 2018) has been fully studied. They studied this event in depth through radio imaging observations, including the three-dimensional magnetic flux rope morphology (Chen et al. 2020a), the variation of magnetic field and electrons along the reconnection current sheet (Chen et al. 2020b), the decay process of magnetic field (Fleishman et al. 2020) and the movement of particles during the gradual phase (Yu et al. 2020). In addition, there are currently two non-solar dedicated low-frequency arrays in the world—LOw Frequency ARray (LOFAR, 10-240 MHz) (van Haarlem et al. 2013) and Murchison Widefield Array (MWA, 80-300 MHz) (Tingay et al. 2013)—which have observed many type III bursts and other FSs. They show us with high frequency, temporal and spatial resolution's solar radio spectrum and imaging observations to study the motion process of non-thermal particles after they propagate into the upper atmosphere (Morosan et al. 2014; McCauley et al. 2017; Cairns et al. 2018).

MingantU SpEctral Radioheliograph (MUSER) is a solar dedicated broadband radio spectral-imaging instrument and began commissioning observation in 2014. Its observational range can completely cover the low-chromosphere to middle-corona areas of the Sun (Yan et al. 2021). We survey the observational data of MUSER from October 2014 to August 2019 and pick out the solar radio burst events as well as making a classification of the FSs following Isliker & Benz (1994); Jiřička et al. (2001); Fu et al. (2004a). Section 2 describes the current status, observational data and the data processing flow of MUSER. Section 3 presents the observational results, statistical Table 1 and Table 2 and the summaries are made in Section 4.

2 INSTRUMENT AND OBSERVATIONAL DATA

MUSER is located in Inner Mongolia of China. It applies synthetic aperture imaging technology that can image the full solar disk in the centimeter-decimeter wavelength range with high frequency, temporal and spatial resolution (Yan et al. 2021). The frequency range of MUSER is from 0.4 to 15 GHz and divided into two sections, MUSER-I (0.4–2 GHz) and MUSER-II (2–15 GHz). MUSER consists of 100 antennas including 40 reflector antennas of 4.5 m diameter (MUSER-I) and 60 reflector antennas of 2.0 m diameter (MUSER-II). The 100 antennas distribute in three spiral arms with the longest baseline of about 3 km. The present study bases on the observational data of MUSER-I. Yan et al. (2016) has introduced the composition of MUSER's system and Du et al. (2015) has introduced the imaging simulations of MUSER-I. It can measure dual circular polarization with 5% accuracy over most of the frequency band (Li et al. 2015, 2016). The frequency and temporal resolution of MUSER-I is 25 MHz and 25 ms, respectively. The dynamic range is 25 dB. MUSER-I uses the $Fengyun\ Satellite$ for phase calibration at 1.6875 and 1.7125 GHz, because the satellite can be regarded as a point source when it is observed on the ground (Wang et al. 2013). The images at other frequencies can be obtained by the self-calibration method based on the images obtained at 1.6875 or 1.7125 GHz. The flux calibration of MUSER images is still under studied. MUSER spectrum does bandpass calibration with the method studied in former works (Yan et al. 2002; Tan et al. 2009, 2015) and the pipeline of calibration is ongoing. MUSER team are considering to use two existed 20 m antennas to observe astronomical sources for phase, flux and bandpass calibration for MUSER-I.

The raw data of MUSER-I adopt user-defined binary format. Every 60 seconds of data are stored as a raw data file including GPS-time, auto-correlation and cross-correlation data, and other information with a size of about 1.8 GB (Wang et al. 2015). At present, there are mainly two ways to process MUSER-I observational data. One is to convert the raw data into measurement set (MS) format and use Common Astronomy Software Applications package (CASA) to obtain radio images (Wang et al. 2015; Mei et al. 2018). The other method is to use programs developed in languages such as Interactive Data Language (IDL), matlab and python to directly read

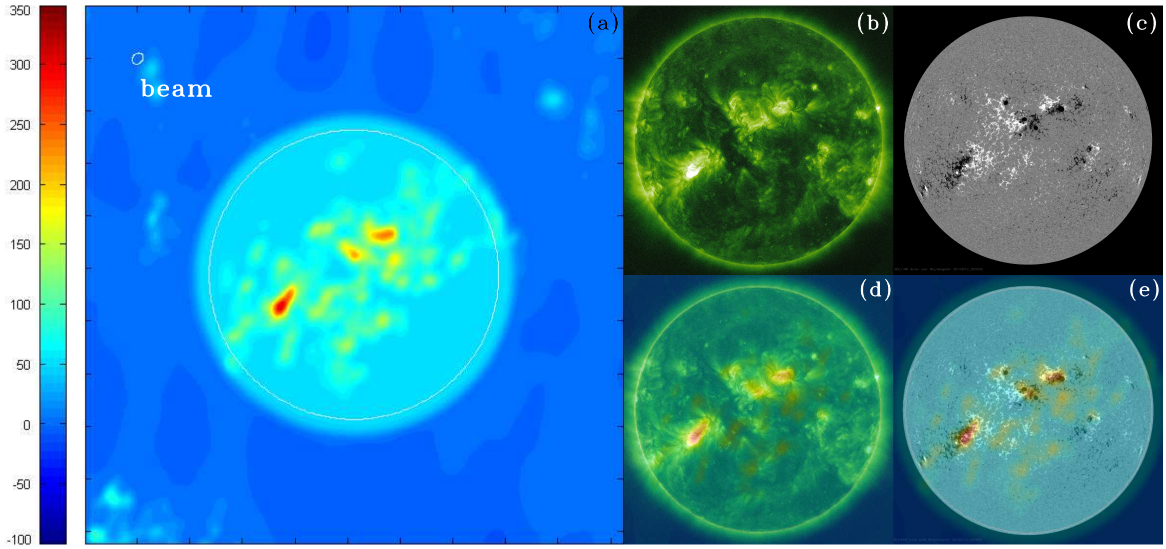

Fig. 1 (a) Quiet solar radio image at 1.7125 GHz observed by MUSER-I array at 5:15 UT on 2014 May 12. The *ellipse* in the upper left corner is the synthesized beam. (b) Corresponding EUV image at 171 Å observed by *SDO*/AIA. (c) Corresponding full-disk LOS magnetogram observed by *SDO*/HMI. (d)/(e) Composite image of (a) and (b)/(c).

Table 1 Statistical Results of FSs of 94 Radio Burst Events Associated with Flares

Type	flare Before	Rise	Decay	After	No flare	Total
Type III-like burst	21	57	23	17	8	126
QPP	3	12	8	1	1	25
Type IV burst	9	25	13	11	4	62
Diffuse continua	1	9	2	1	3	16
Spike	3	13	5	5	0	26
Lace	0	4	1	1	0	6
Fiber	1	2	1	3	0	7
Unusual	1	8	3	2	0	14
Total	39	130	56	41	16	282

the raw data file and do Fourier transform to obtain the radio images (Chen et al. 2019). We have verified that both methods can obtain the same results.

The daily observational data were classified into data with or without radio bursts for further storage due to the storage space limitations before 2019. During the early period of the routine observation, the MUSER team saved data based on *Geostationary Operational Environmental Satellites* (*GOES*) soft X-ray (SXR) flare. The raw data was saved when the SXR flare equal to or larger than B-class, otherwise the data were reduced to the temporal resolution of one minute. With the development of data analysis, after 2017, the team checked radio flux at several fixed frequencies to determine whether there were radio bursts in the observational data or not. If there is a radio burst, the team would save the raw data throughout the day. Meanwhile, some data of the quiet Sun are also saved when the instrument is in a good condition. At present, all raw data are saved as the data storage capacity has been greatly improved after the permanent buildings were constructed at Mingantu Observing Station in 2019.

3 OBSERVATIONAL RESULTS

3.1 Observational Results of Quiet Sun

We take the quiet solar radio imaging at 5:15 UT on 2014 May 12 as an example. Figure 1(a) shows an image recorded at 1.7125 GHz. A synthesized beam with the full-width at half-maximum (FWHM) of about 60″, which is used for restoring the deconvolved synthesis images, is shown in the upper left corner. The unit of intensity is in arbitrary unit with colorbar on the left side. Seventeen antennas (a total of 136 baselines after removing bad baselines) are used to image the Sun, due to the maintenance of several antennas on the day. A quiet Sun disk model is applied to the image similar to other radioheliographs (Nakajima et al. 1995), and the integration time is 30 ms. Figure 1(b) is the extreme ultraviolet (EUV) image at 171 Å observed by *Solar Dynamics Observatory* (*SDO*)/Atmospheric Imaging Assembly (AIA; Lemen et al. 2012) and Figure 1(c) is the full-disk line-of-sight (LOS) photospheric magnetogram observed by *SDO*/ Helioseismic and Magnetic Imager (HMI; Scherrer et al. 2012). Figure 1(d) and (e) are composite images with yellow and red for radio image (Fig. 1(a)), green for 171 Å EUV image (Fig. 1(b)), and gray scale for HMI magnetogram (Fig. 1(c)) of *SDO*, respectively. Both images show that radio source regions are correspond to the structure of EUV active regions. The quiet solar image shown here is to demonstrate the imaging capability and performance of MUSER.

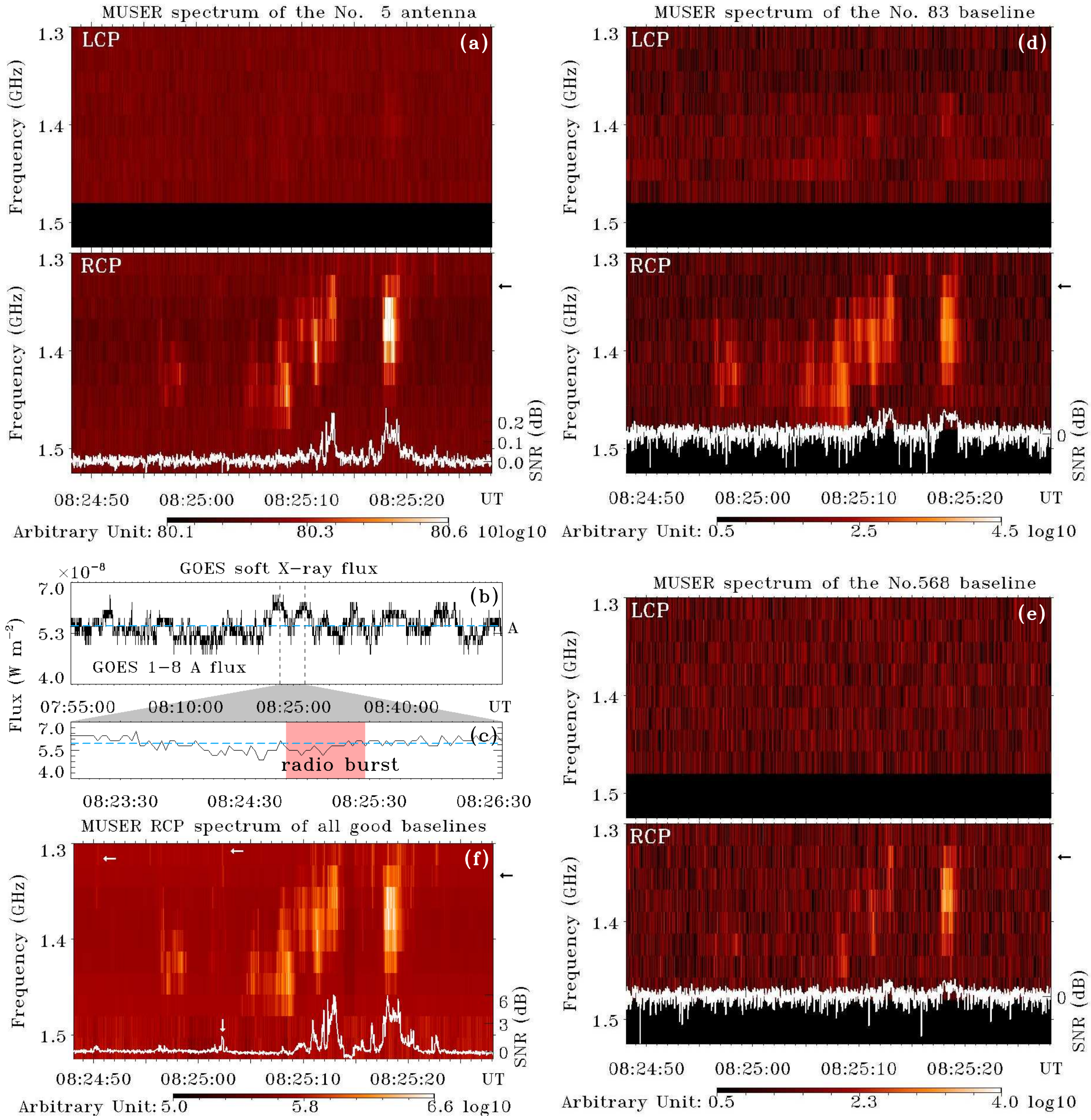

Fig. 2 (a) MUSER auto-correlation dynamic spectrum of No.5 (A4) antenna. (b) The SXR intensity observed by *GOES* from 07:55 to 08:55 UT on 2017 June 22. (c) The SXR intensity between the two *dashed lines* in (b). (d)–(e) Corresponding cross-correlation dynamic spectrum of No.83 and No.568 baselines, respectively. (f) The total intensity of all good (168) RCP baselines.

Quantitative analysis of the quiet Sun could be achieved after the flux calibration.

3.2 Observational Results of Radio Bursts

We check all the raw data of MUSER-I from October 2014 to August 2019 to identify the radio burst events. First, we select the data with radio bursts by browsing auto-correlation spectrum with the temporal and frequency resolution of 25 ms and 25 MHz. Second, we check the cross-correlation spectrum of these bursts to preclude interference signals. A radio burst can be determined when its signal is larger than three times of the mean square deviation for a quiet time period of the Sun of about one minute. Finally, we find a total of 94 radio burst events in about 300 TB of all raw data. These events contain abundant FSs including QPPs, spikes, laces and so on.

It is usually believed that most solar radio burst events are associated with flares, so we check the possible associated flare information by using the detection data of *soft X-ray telescope* on *GOES* (`http://www.swpc.noaa.gov/products/goes-x-ray-flux`) and the SXR intensity curve corresponding to each radio burst event. We stipulate that it implies a flare occurs when the SXR intensity has a sudden increase. Many studies have shown that there will

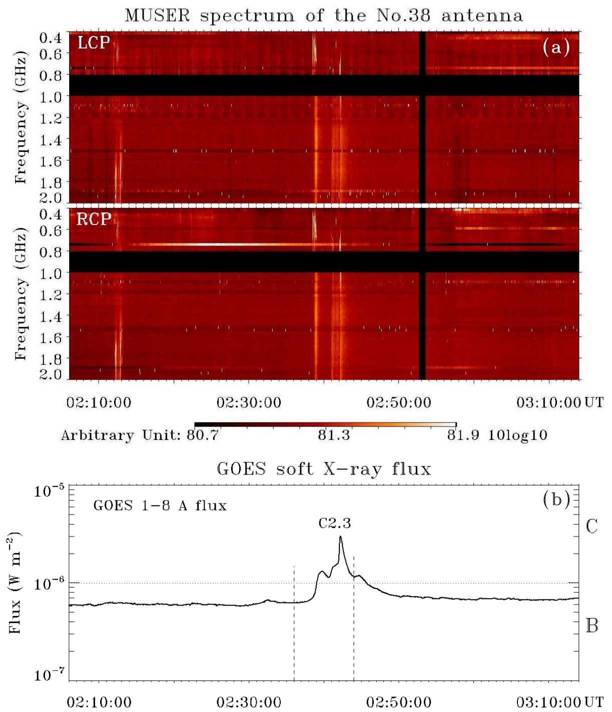

Fig. 3 (a) MUSER auto-correlation dynamic spectrum of the No.38 (C11) antenna. (b) The SXR intensity observed by *GOES* from 2:06 to 3:14 UT on 2015 June 20. The *black dashed lines* are the start and stop time of the C2.3 flare.

be radio bursts before the start and after the stop time of flares (e.g., Kundu & Vlahos 1982; Willson et al. 1990; Xie & Wang 2000; Zhang et al. 2015; Tan et al. 2016). In addition, Xie et al. (1994) found that out of 76 radio burst events, 23 events showed a flux increase at least in one of the four frequencies (1.42, 2.13, 2.84 and 4.26 GHz) before the flare onsets by a time range from several to tens of minutes. Kai et al. (1983) studied 97 bursts recorded by the Nobeyama interferometer at 17 GHz, they found that 26% of the bursts would have smaller bursts between 10 and 35 min before the main bursts. Therefore, we classify the independent radio bursts within 30 min before the start and after the stop time of the flare as the same activity with the main radio bursts which occurred during the flaring time. As a result, we find that there are 81 radio burst events accompanied with flares in the total of 94 radio burst events and the rest 13 radio burst events without accompanying corresponding flares (the SXR intensity did not show a sudden increase). While for these 13 events, SXR intensity levels during the radio bursts time period are also given to help readers to understand the radio bursts occurring. Yan et al. (2016) reported a radio burst event observed by MUSER-I array during 4:22–4:24 UT on 2014 November 11 — the first event listed in Table 2. They found that during the radio burst,

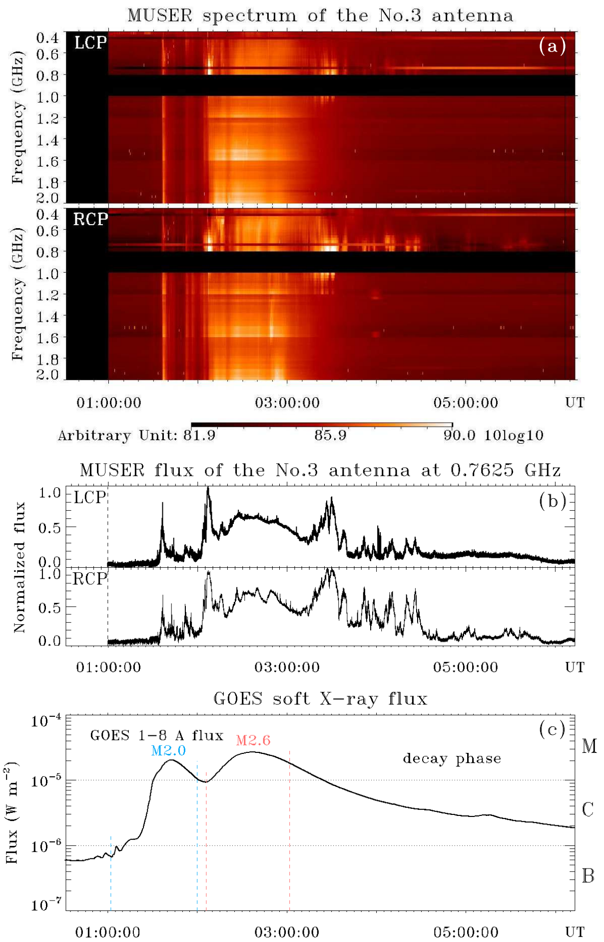

Fig. 4 (a) MUSER auto-correlation dynamic spectrum of the No.3 (A2) antenna. (b) MUSER auto-correlation flux of the No.3 (A2) antenna at 0.7625 GHz. (c) The SXR intensity observed by *GOES* from 0:32 to 6:13 UT on 2015 June 21. The *blue*/*red dashed lines* are the start and stop time of the M2.0/M2.6 flare.

there was a C3.4 flare started from 4:22 UT and peaked at 4:49 UT in the solar disk center, whereas the radio burst source was located at the east limb of the Sun. Therefore, considering that the main purpose of this article is to summarize the observations of MUSER in the past 5 years and give an event list for further studies, we mainly give information about the dynamic spectra of radio bursts and possible related SXR flares from the temporal relationship here. The detailed MUSER imaging and analyses of these radio bursts will be provided in future studies. We provide four examples to show our classification in the following subsection.

3.2.1 Radio bursts on 2017 June 22

A radio burst event which occurred at 08:24:50 UT on 2017 June 22 and lasted about 35 s was observed by MUSER-I array. Figure 2(a) is MUSER auto-correlation

Table 2 Observational Results of Solar Radio Bursts

Event	Start	Stop	III-like	QPP	IV	Dif	Spi	Lac	Fib	Unu	Class/Level
2014 Nov 11	3:59(3:28)	4:00(4:32)	✓								C1.1
	4:16(4:11)	5:05(5:26)	✓	✓		✓					C3.4
	5:32(5:02)	5:53(6:04)	✓	✓							C2.1
	6:13(6:02)	6:30(7:14)	✓	✓							C3.1
	7:59(7:27)	8:00(8:41)	✓								C2.3
2014 Dec 17	1:46(1:11)	2:27(2:27)			✓				✓		M1.1
	4:22(3:55)	5:22(5:50)	✓	✓	✓	✓	✓	✓	✓		M8.7
2015 May 21	5:55(4:52)	5:57(6:23)	✓								B6.3
2015 Jun 20	1:13(0:51)	1:25(2:00)			✓			✓			B6.9
	2:08(2:06)	2:42(3:14)	✓	✓		✓					C2.3
2015 Jun 21	1:17(0:32)	6:13(3:32)	✓	✓	✓		✓	✓	✓	✓	M2.0 M2.6
2015 Nov 4	3:57(3:23)	4:04(4:35)	✓								C1.4
	4:52(4:20)	4:56(5:29)	✓								C1.0
2015 Nov 22	4:51(4:21)	4:53(5:30)	✓								C1.1
	5:35(5:01)	5:38(6:11)	✓								C5.6
2016 Aug 29	3:44(3:04)	3:50(4:32)								✓	C2.2
2016 Sep 22	3:26(2:53)	3:27(4:02)	✓								B4.7
2016 Nov 29	7:07(6:33)	7:09(7:42)	✓								C7.5
2017 Feb 28	6:28(5:53)	6:30(7:02)	✓								B3.5
2017 May 1	3:58(3:25)	4:00(4:35)	✓								B9.9
2017 Jun 2	1:31(0:59)	1:48(2:21)	✓							✓	B8.5 C1.1
	9:49(9:17)	9:51(10:26)	✓								B4.6
2017 Jun 3	4:08	4:10	✓			✓					level-B
	9:37(9:07)	9:55(10:35)	✓			✓					C2.1
2017 Jun 22	8:24	8:26	✓								level-A
2017 Jul 10	1:23	1:26			✓						level-B
	3:51(3:39)	5:06(7:20)	✓		✓						B5.4
	9:48	9:53			✓						level-B
2017 Jul 12	8:18	8:25			✓						level-B
2017 Jul 14	1:18(0:37)	2:50(3:54)	✓		✓		✓	✓			M2.4
2017 Jul 16	1:58(1:28)	2:11(3:27)	✓		✓	✓					C3.1
2017 Jul 17	7:24(7:13)	7:25(8:16)	✓								B3.3
2017 Aug 15	4:30(3:54)	4:33(5:03)	✓								B8.7
	5:05(4:30)	5:07(5:39)	✓								B7.1
2017 Aug 16	8:27(7:59)	8:34(9:10)	✓				✓				B5.2
2017 Aug 20	1:57(1:06)	2:00(2:33)	✓								M1.1
2017 Aug 21	2:30(1:59)	2:32(3:12)	✓								B7.3
2017 Aug 22	4:00(3:45)	4:30(4:54)	✓		✓						B6.2
	8:31(8:01)	8:37(9:09)	✓		✓					✓	B5.5
2017 Aug 23	6:25(5:54)	6:27(7:27)	✓								C1.6
2017 Aug 24	4:29(3:59)	4:33(5:03)								✓	B1.8
2017 Aug 25	7:24(6:45)	7:28(8:16)	✓		✓	✓					C5.5
2017 Sep 4	1:11	1:12	✓								level-C
	2:11(1:48)	2:23(2:59)	✓								C1.1
2017 Sep 5	4:43(4:03)	4:47(5:37)			✓						M3.2
	6:40(6:03)	7:08(7:13)			✓					✓	M3.8
2017 Sep 6	7:31(6:59)	7:39(8:18)	✓	✓						✓	C2.7
	8:49(8:27)	9:16(9:47)	✓	✓	✓	✓				✓	X2.2
2017 Sep 7	2:00(1:31)	2:03(2:33)	✓		✓		✓				C1.8
	2:52(2:23)	2:55(3:30)								✓	C2.3
	5:32(4:29)	5:38(5:38)	✓							✓	M2.4
	6:17(5:49)	7:11(7:12)	✓	✓	✓		✓				C8.2
	7:25(7:03)	7:49(8:06)	✓		✓					✓	C3.7
	8:22(8:02)	8:39(9:07)	✓	✓	✓		✓				C1.7
	9:16(8:46)	9:28(9:54)	✓		✓		✓				C2.3
2017 Sep 8	1:25(1:06)	1:47(2:12)	✓	✓	✓		✓				C5.3
	2:11(1:40)	2:14(2:45)	✓	✓	✓						C1.2
	2:30(1:49)	2:59(2:59)	✓		✓		✓				M1.3
	3:27(3:00)	3:35(4:07)	✓		✓					✓	C1.4
	3:39(3:09)	3:47(4:15)	✓	✓	✓						M1.2
	4:20	4:56	✓		✓						level-C
	5:08(5:01)	6:57(7:11)	✓	✓	✓		✓				C8.3 C2.9 C1.7
	7:03(6:34)	7:11(7:40)	✓	✓	✓		✓				C6.0
	7:20(7:10)	9:32(8:28)	✓		✓		✓		✓		M8.1
	9:36(9:06)	9:39(10:11)	✓		✓						C1.3
2017 Sep 9	5:14	5:19	✓	✓							M1.1 in decay phase
	6:52(6:21)	6:57(7:28)	✓		✓	✓					C1.7

Table 2 *Continued.*

Event	Start	Stop	III-like	QPP	IV	Dif	Spi	Lac	Fib	Unu	Class/Level
2017 Sep 10	2:54(2:10)	2:56(3:55)	✓								C9.0
	4:38	4:40	✓								C9.0 in decay phase
2017 Sep 11	3:07(2:34)	3:11(3:38)	✓								C2.0
2017 Sep 12	7:24(6:52)	7:30(8:04)	✓		✓	✓			✓		C3.0
2017 Sep 13	5:39(5:08)	5:51(6:21)	✓		✓		✓				B1.1
2017 Sep 14	0:57(0:35)	1:05(1:40)	✓								B1.0
2017 Sep 24	8:22(7:51)	8:23(8:54)	✓								B2.6
2017 Sep 26	2:33(1:59)	2:36(3:08)	✓	✓							C1.8
2017 Oct 7	2:21(1:49)	2:23(2:58)	✓								B4.9
	8:33	8:35	✓								level-B
2017 Oct 18	5:33	5:36				✓					level-A
	7:41	7:47				✓					level-A
2018 Mar 24	4:34	4:35	✓								level-A
2018 Mar 30	4:11(3:41)	4:18(4:49)	✓								B1.8
	4:47(4:37)	5:16(5:51)	✓								B4.5
	7:59(7:27)	8:06(8:38)	✓		✓						C4.6
2019 May 5	6:38(6:07)	6:44(7:14)	✓				✓				B2.3
2019 May 6	5:01(4:34)	5:12(5:42)	✓	✓							C9.9
	6:23(5:45)	6:25(6:50)	✓								B2.1
	8:10(6:53)	8:54(9:21)	✓								C1.7 C2.0
2019 May 7	1:40(1:08)	1:47(2:18)	✓			✓					B6.5
	2:53(2:20)	2:54(3:23)	✓								B2.0
	3:18(3:13)	3:20(4:22)	✓								B2.4
	4:51(4:22)	4:54(5:30)	✓								B3.4
	5:36(5:09)	5:40(6:10)	✓								B1.8
	7:22(6:48)	7:26(7:57)	✓								B3.1
2019 May 9	5:43(5:10)	6:04(6:26)	✓			✓					C6.7

Notes: Event - date of the solar radio burst events; Start and stop time is universal time; III-like - type III-like burst; QPP - quasi-periodic pulsation; IV - type IV burst; Dif - diffuse continua; Spi - spike; Lac - lace; Fib - fiber; Unu - unusual burst; Class/Level - the flare class of a radio burst event accompany with flare(s) or the SXR intensity level of an independent radio burst event.

dynamic spectrum of No. 5 (A4) antenna. It shows a typical narrowband type III burst with strong right circle polarization (RCP). Figure 2(b) shows the *GOES* SXR intensity variation during the time period from 07:55 to 08:55 UT, which shows no obvious intensity increase for a total of 60 min before and after the radio burst period, although the SXR intensity fluctuations covering the radio bursts' period may indicate some certain associations between them. The intensity is shown in logarithm scale. The blue long dashed line indicates the average intensity during this period is 5.51×10^{-8} W m^{-2}. Figure 2(c) is the SXR intensity corresponding to the time period of 5 min between the two dashed lines in Figure 2(b) and the intensity is shown in ordinate. The average intensity during this 5 min is 5.86×10^{-8} W m^{-2}. The red shadow area indicates the time period with the radio burst event as shown in Figure 2(a). The SXR intensity during the radio burst event is basically below the average intensity. As shown in Figure 2(b), the maximum SXR intensity during the radio burst is level-A6.5. Figures 2(d) and 2(e) are the cross-correlation dynamic spectrum of No.83 baseline (No.3 (A2) and No.9 (A8) antenna, 245.7 m) and No.568 baseline (No.19 (B5) and No.38 (C11) antenna, 702.3 m), respectively. There are 168 good baselines in this event. Figure 2(f) is the total intensity of all good baselines, which reduced the noise. The areas pointed by the two white horizontal arrows show weaker signal of the FSs than auto- and cross-correlation dynamic spectrum of which we do not see significant radio signals in the same areas. We calculated the Signal to Noise Ratio (SNR) with $\mathrm{SNR} = 10 \lg \frac{P_\mathrm{s}}{P_\mathrm{n}}$. Here P_s and P_n are the effective power of signal and noise respectively. The white curves in Figures 2(c), 2(d), 2(e) and 2(f) represent the RCP SNR of 1.3375 GHz (the position marked by the black arrow) with the axis on the right side. The highest SNR in the areas pointed by the two white horizontal arrows at 1.3375 GHz in Figure 2(f) is 1.7 dB (pointed by the vertical arrow), but no obvious peaks are seen at the same position in Figures 2(c), 2(d) or 2(e).

3.2.2 *Radio bursts on 2015 June 20*

Figure 3(a) shows the second example with MUSER auto-correlation dynamic spectrum of the No.38 (C11) antenna. It shows that a radio burst occurred from 2:38:28 to 2:42:21 UT on 2015 June 20. Meanwhile, we find that about 25 min before this major burst, there is anther radio burst which occurred from 2:09:19 to 2:13:11 UT. Both radio bursts occurred at the similar frequency range and with no obvious polarization. A C2.3 flare occurred from 2:36 to 2:46 UT according to *GOES* records. It is co-temporal with the major radio burst which occurred during the time period from 2:38:28 to 2:42:21 UT. We extend the start

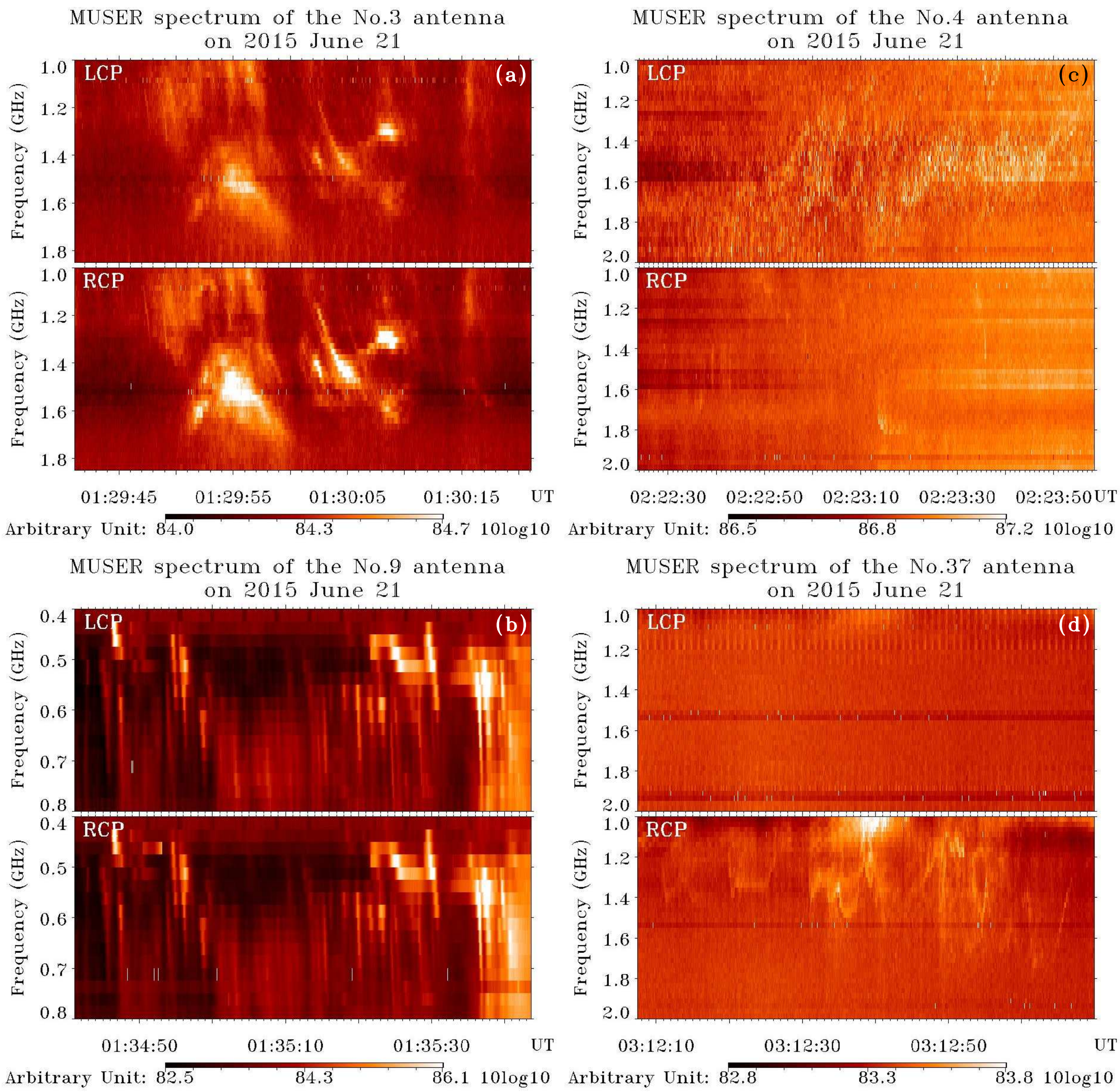

Fig. 5 (a) Unusual bursts. (b) Narrowband type III bursts. (c) Spike bursts. (d) Lace bursts.

time of the C2.3 flare (2:36 UT) forward by 30 min (2:06 UT), the stop time (2:46 UT) backward by 30 min (3:14 UT), and show the *GOES* SXR intensity during this period in Figure 3(b). The dashed lines indicate the start and stop time of the flare, respectively. The radio burst at 2:09:19 UT are within 30 min before the start of C2.3 flare. Therefore, we classify this kind of radio bursts as pre-flare activities according to the classification rules for radio bursts mentioned above.

3.2.3 *Radio bursts on 2015 June 21*

The third example is the radio burst event which occurred from 1:17:27 to 6:13:04 UT on 2015 June 21. Figures 4(a) shows the auto-correlation dynamic spectrum of No.3 (A2) antenna. Figures 4(b) is the intensity variation at 0.7625 GHz. Both dynamic spectrum and flux show that the radio bursts last for a long time and the radio flux return back to the background level till around 6:13 UT. Figure 4(c) is *GOES* SXR intensity on 2015 June 21. There are two flares which defined as M2.0 and M2.6 during the radio bursts according to *GOES* records. The dashed lines of the same color in Figure 4(c) indicate the start and stop time of the corresponding flare, respectively. We extend the start time of M2.0 flare (1:02 UT) forward by 30 min (0:32 UT) and the stop time of M2.6 flare (3:02 UT) backward by 30 min (3:32 UT). The time period from 0:32 to 0:59 UT correspond to 8:32 to 8:59 in Beijing Time. MUSER has not yet started to observe during that period. In order to

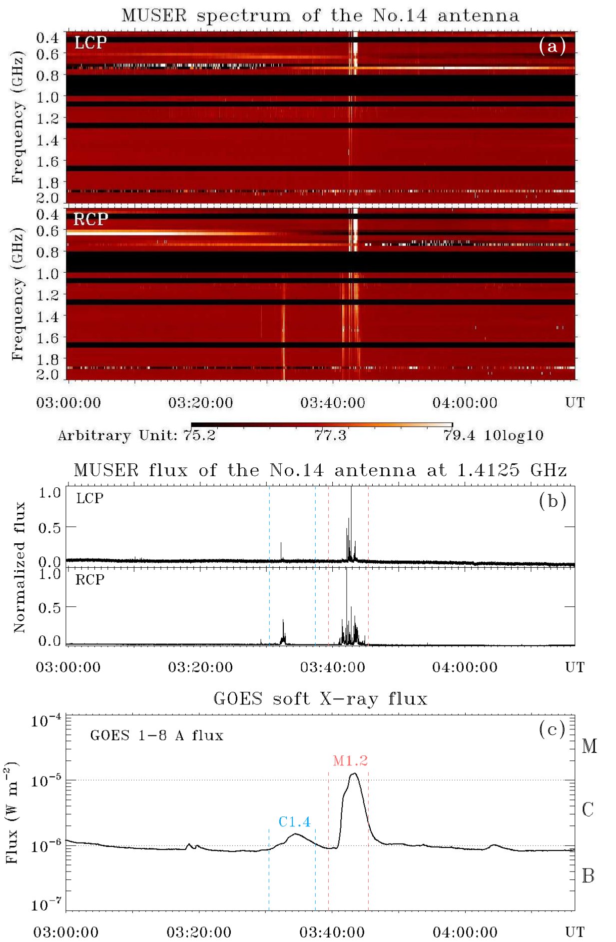

Fig. 6 (a) MUSER auto-correlation dynamic spectrum of the No.14 (A13) antenna. (b) MUSER flux of the No.14 (A13) antenna at 1.4125 GHz. (c) The SXR intensity observed by *GOES* from 3:00 to 4:15 UT on 2017 September 8. The *blue*/*red dashed lines* are the start and stop time of the C1.4/M1.2 flare.

keep the time axis consistent, we set the spectrum and flux value of this period to zero (black), which are the black areas in Figure 4(a) and blank areas in Figure 4(b). As shown in Figure 4(c), the M2.6 flare also has a long decay phase with the intensity still in level-C till 6:13 UT. It is still higher than the background intensity at level-B before the start of the M2.0 flare. Meanwhile, the intensity begin to rise again before the M2.0 flare fall to the background intensity level and the radio bursts on spectrum (Fig. 4(a)) is continuous. The specific location of the radio bursts cannot be determined since imaging analysis have not yet been carried out. We count the radio bursts from 1:17:27 to 6:13:04 UT as one radio burst event accompanying two (M2.0 and M2.6) flares and classify this kind of events as radio burst events accompanying more than one flare.

Figure 5 shows some examples of the auto-correlation dynamic spectrum of FSs observed by MUSER-I array in the long-duration burst event on 2015 June 21. Figure 5(a) is an unusual burst at 1:29:47 UT. Their average frequency drifts are +89.2 $\mathrm{MHz\ s^{-1}}$. Figure 5(b) is narrowband type III bursts with positive frequency drift at 1:34:45 UT, the average frequency drifts of bursts is +320.9 $\mathrm{MHz\ s^{-1}}$. Figure 5(c) is spike bursts with strong left circle polarization at 2:32:24 UT and Figure 5(d) is lace bursts with strong RCP at 3:12:11 UT.

3.2.4 Radio bursts on 2017 September 8

Here we show the last example with two radio burst events occurred within 18 min on 2017 September 8, which are accompanied with C1.4 and M1.2 flares respectively. Figure 6(a) is auto-correlation dynamic spectrum of the No.14 (A13) antenna. It shows a fully polarized (2:28:12 to 3:34:18 UT) and a partially polarized (3:39:50 to 3:46:14 UT) radio burst event. Figure 6(b) is MUSER flux of the No.14 (A13) antenna at 1.4125 GHz and Figure 6(c) is the SXR intensity observed by *GOES* on 2017 September 8. The dashed lines of the same color indicate the start and stop time of the corresponding flare respectively. All time axes are extended from the start time of C1.4 flare (3:30 UT) forward by 30 min (3:00 UT) to the stop time of M1.2 flare (3:45 UT) backward by 30 min (4:15 UT). The SXR intensity has dropped to the background intensity level around 3:39 UT as shown in Figure 6(c). Meanwhile, the time distribution of radio bursts is obviously two separate parts which co-temporal with two flares, respectively. That is, the radio bursts around 3:30 and 3:40 UT are obviously accompanied with two different flares. We count them as two radio bursts, although the time interval of the two flares is only 10 min and classify them as radio burst events accompanying one flare for this kind of events.

3.2.5 Statistical results

The statistical results of all FSs of 94 radio burst events are given in Table 1. The types of FSs include type III-like bursts, QPPs, type IV bursts, diffuse continua bursts, spikes, lace bursts, fibers and some unusual bursts. Unusual bursts are collections of various FSs that are not in the above classification. Figures 5 and 7 show typical examples for each burst type. Figure 7(a) is QPPs with strong RCP at 5:32:51 UT on 2014 November 11. Figure 7(b) is fibers superimposed on type IV continua with strong RCP at 5:05:22 UT on 2014 December 17. The total bandwidth and duration are 400 MHz and 5.2 s, respectively. The average frequency drift of fiber is –104.03 $\mathrm{MHz\ s^{-1}}$. Figure 7(c) is broadband type III bursts with the bandwidth is 600 MHz at 3:58:11 UT on 2015 November 4 and Figure 7(d) is diffuse continua bursts with strong RCP at 4:38:28 UT on 2014 December 17.

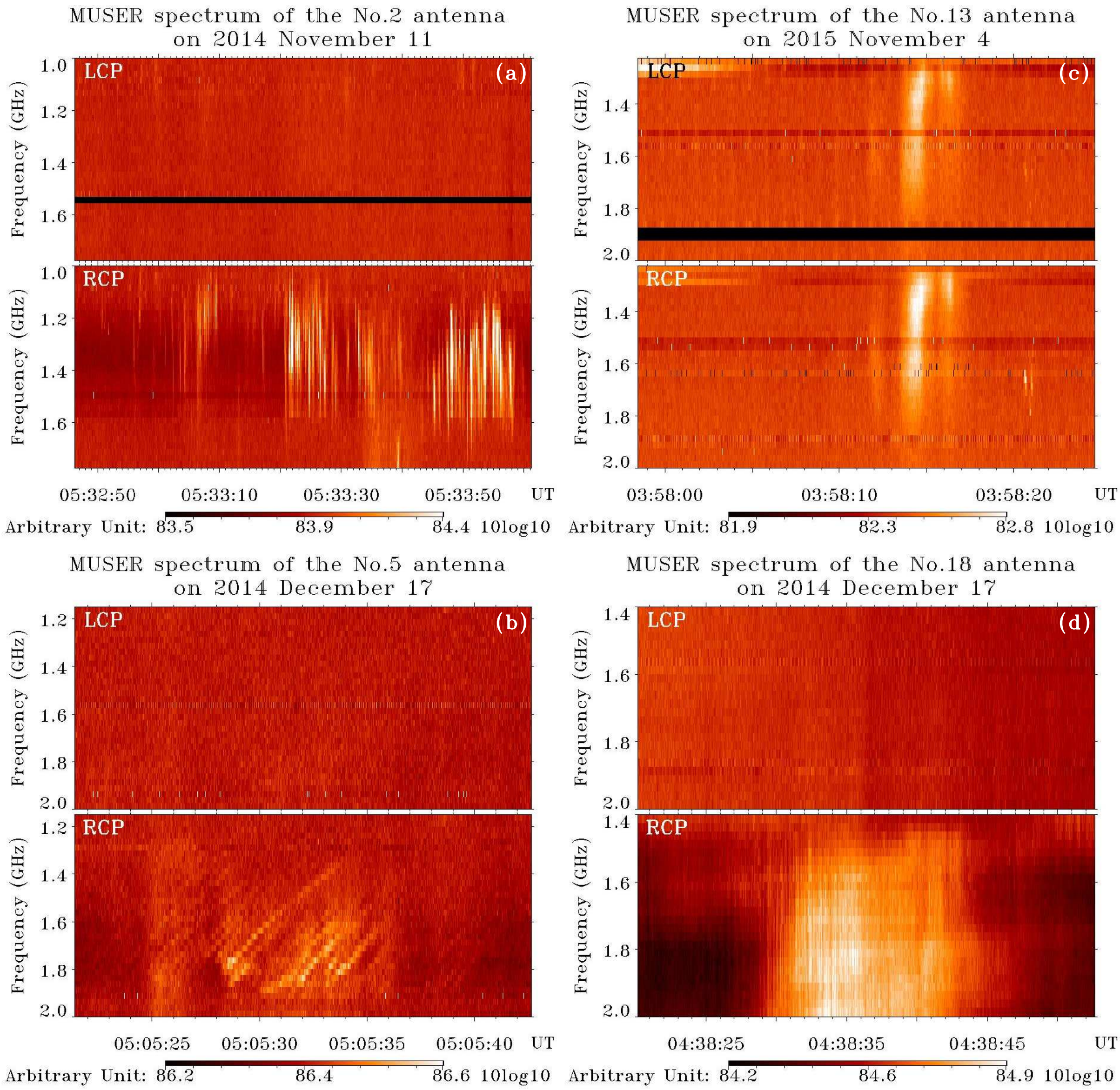

Fig. 7 (a) QPPs. (b) Fibers superimposed on type IV continua. (c) Broadband type III bursts. (d) Diffuse continua bursts.

In a total of 94 radio burst events, 81 radio burst events occur accompanied with flares and the other 13 radio burst events not. For the FSs of radio burst events associated with flares, we subdivide their occurrence time into four phases according to the associated flares, including the pre-flare phase (before), the impulsive phase (rise), the decay phase (decay) and post-flare phase (after). Regarding the FSs of radio burst events accompany no flares, we classify them as a category—no flare. As shown in Table 1, the total amount of radio FSs are 282. The results indicate that the type III-like bursts (up to 126) are the most common FSs, lace bursts (only 6) are the least frequent FSs among 94 events and flare-associated (81 radio events) FSs mostly occur at impulsive phase (130 in total).

Table 2 is the observational results of 94 radio burst events. The start and stop time without brackets in Table 2 indicate the start and stop time of the dynamic spectrum of radio burst events observed by MUSER-I. The start and stop time in brackets in Table 2 indicate the start and stop time of the corresponding flare in the flare event list with extended forward and backward by 30 min. For the 81 events which associated with flares, 77 of them accompany with one flare, including 29 B-, 37 C-, 10 M- (1 event extend to decay phase—the last radio burst event on 2017 September 8 in Table 2), and 1 X-class flare and 4 of them are accompanied with more than one flare, including 1 B-, 6 C-, and 2 M- (1 event extend to decay phase—the radio burst event on 2015 June 21 in Table 2) class flares. Moreover, we also count the intensity level of *GOES* SXR intensity during the radio bursts for the 13 independent radio burst events to make it easier to understand, including 4 level-A, 5 level-B, 3 level-C and 1 level-M. For the independent radio bursts, we find that there are two radio burst events which occurred during the flare decay phase with high SXR intensity after the flare stop. The one occurred around 5:14–5:19 UT, 2017 September 9. *GOES* records an M1.1 flare which starts at 4:14 UT and stops at 4:43 UT. The dynamic spectrum of MUSER did not show radio bursts during the M1.1 flare or within 30 minute after the stop of the flare, but showed a radio burst from 5:14 to 5:19 UT when *GOES* SXR intensity at level-C and continues to decline. The other event occurred around 4:38–4:40 UT, 2017 September 10. A C9.0 flare started at 2:40 UT, stopped at 3:25 UT and SXR intensity continued to decline until around 6:00 UT. MUSER recorded a radio burst event (2:54 to 2:56 UT) during the C9.0 flare and 104 min later, it observed this event (4:38 to 4:40 UT) during C9.0 flare decay phase.

Among the 81 radio burst events which accompanied with flares, we find 20 radio burst events with pre-flares activities and the interval between the pre-flare activities and the main bursts range from 1 to 28 min with an average of 12.1 min. For the pre-flare radio bursts, the most common types of FS are type III-like bursts and type IV bursts. More details of each radio burst event are listed in Table 2. We find that the higher of the flare class (or SXR intensity level), the more abundant FS types of radio burst events.

4 SUMMARIES

Solar radio burst is an important field in solar physics research. MUSER as the latest generation of solar-dedicated spectral radioheliograph, has unique high frequency, temporal and spatial resolution and a wide wavelength range. The measuring range of MUSER can completely cover the low-chromosphere to middle-corona areas of the Sun, helping us to understand the physics mechanism of kinds of solar activities. Meanwhile, the MUSER observational data processing method has been gradually improved after several years of optimization and the data processing process has become simpler and faster, providing a very good foundation for us to use and research.

We have obtained very good images of the quiet Sun of MUSER-I at 1.7125 GHz, and the full disk of the Sun can be seen through proper integration. MUSER-I array has recorded 94 radio burst events with abundant FSs in nearly 5 years, including all kinds of type III bursts (narrowband type III bursts, broadband type III bursts, regular type III bursts and reversed-drift type III bursts), QPPs, type IV bursts, diffuse continua bursts, spikes, lace bursts, fibers and some unusual bursts. We find: 1) 86.17% of radio burst events are accompanied with flares and 13.83% of radio burst events are independent radio bursts. 2) Among 81 radio burst events which accompanied with flares, 20 events have pre-flare activities and the average time before the start of flare is 12.1 min. In precending radio bursts, the most common types of FS are type III-like bursts and type IV bursts. 3) The higher of the flare class (or SXR intensity level), the more abundant FS types of the radio burst events. 4) The type III-like bursts are the most common FSs and lace bursts are the least frequent FSs among 94 events and flare-associated (81 radio events) FSs mostly occur at the rise phase.

This work gives the summary of observational results of MUSER-I. In-depth statistical analysis and further individual cases including imaging and spectral analyses of these 94 radio burst events will be made later. Many radio burst events have been recorded since MUSER-I array formally observation in 2014, including four radio burst events corresponding to level-A SXR intensity which show that the sensitivity of MUSER-I is very good. MUSER will be able to play a huge role in capturing the valuable information of solar nonthermal processes and importance for space weather on the occasion of solar cycle 25.

Acknowledgements The authors are thankful for the teams of *SDO*/AIA, *SDO*/HMI and *GOES*/SXR for providing the relevant data. In addition, we thank the reviewers for their thoughtful suggestions that have helped improve this paper substantially. This work is supported by the National Natural Science Foundation of China (Grant Nos. 11790301, 11790305, 11973057, 12003048, 11903055, 11773043 and 12003049). This work is also supported by the Ministry of Science and Technology of China Key Project (2018YFA0404602) and the international collaboration of ISSI-BJ.

References

Altyntsev, A. T., Kuznetsov, A. A., Meshalkina, N. S., & Yihua, Y. 2003, A&A, 411, 263
Aschwanden, M. J., Benz, A. O., Dennis, B. R., & Schwartz, R. A. 1995, ApJ, 455, 347
Bastian, T. S., Benz, A. O., & Gary, D. E. 1998, ARA&A, 36, 131
Bouratzis, C., Hillaris, A., Alissandrakis, C. E., et al. 2015, Sol. Phys., 290, 219
Bouratzis, C., Preka-Papadema, P., Moussas, X., et al. 2009, Advances in Space Research, 43, 605
Cairns, I. H., Lobzin, V. V., Donea, A., et al. 2018, Scientific Reports, 8, 1676
Chen, B., Bastian, T. S., Shen, C., et al. 2015, Science, 350, 1238
Chen, B., Bastian, T. S., White, S. M., et al. 2013, ApJL, 763, L21

Chen, B., Yu, S., Reeves, K. K., & Gary, D. E. 2020a, ApJL, 895, L50
Chen, B., Shen, C., Gary, D. E., et al. 2020b, Nature Astronomy, 4, 1140
Chen, X., Yan, Y., Tan, B., et al. 2019, ApJ, 878, 78
Chernov, G. 2011, Fine Structure of Solar Radio Bursts (Berlin: Springer)
Chernov, G. P. 2010, RAA (Research in Astronomy and Astrophysics), 10, 821
Du, J., Yan, Y., Wang, W., & Liu, D. 2015, PASA, 32, e024
Dulk, G. A. 1985, ARA&A, 23, 169
Fleishman, G. D., Gary, D. E., Chen, B., et al. 2020, Science, 367, 278
Fu, Q.-J., Yan, Y.-H., Liu, Y.-Y., et al. 2004a, ChJAA (Chin. J. Astron. Astrophys.), 4, 176
Fu, Q., Ji, H., Qin, Z., et al. 2004b, Sol. Phys., 222, 167
Gary, D. E., Chen, B., Dennis, B. R., et al. 2018, ApJ, 863, 83
Hey, J. S. 1946, Nature, 157, 47
Huang, G., & Nakajima, H. 2005, Ap&SS, 295, 423
Huang, J., Yan, Y., & Liu, Y. 2007, Advances in Space Research, 39, 1439
Isliker, H., & Benz, A. O. 1994, A&AS, 104, 145
Jiricka, K., Karlicky, M., Kepka, O., & Tlamicha, A. 1993, Sol. Phys., 147, 203
Jiřička, K., Karlický, M., Mészárosová, H., & Snížek, V. 2001, A&A, 375, 243
Kai, K., Nakajima, H., & Kosugi, T. 1983, PASJ, 35, 285
Karlický, M., Bárta, M., Jiřička, K., et al. 2001, A&A, 375, 638
Kundu, M. R., & Vlahos, L. 1982, Space Sci. Rev., 32, 405
Lemen, J. R., Title, A. M., Akin, D. J., et al. 2012, Sol. Phys., 275, 17
Li, S., Yan, Y. H., Chen, Z. J., et al. 2015, PASA, 32, e013
Li, Y., Zheng, J., Tuthill, P., et al. 2016, PASA, 33, e008
Maxwell, A., & Thompson, A. R. 1962, ApJ, 135, 138
McCauley, P. I., Cairns, I. H., Morgan, J., et al. 2017, ApJ, 851, 151
Mei, Y., Wang, F., Wang, W., et al. 2018, PASP, 130, 014503
Morosan, D. E., Gallagher, P. T., Zucca, P., et al. 2014, A&A, 568, A67
Nakajima, H., Nishio, M., Enome, S., et al. 1995, Journal of Astrophysics and Astronomy Supplement, 16, 437
Ning, Z.-j., Fu, Q.-j., & Lu, Q.-k. 2000, Chinese Astronomy and Astrophysics, 24, 359
Nita, G. M., Hickish, J., MacMahon, D., & Gary, D. E. 2016, Journal of Astronomical Instrumentation, 5, 1641009
Reid, H. A. S., & Ratcliffe, H. 2014, RAA (Research in Astronomy and Astrophysics), 14, 773
Scherrer, P. H., Schou, J., Bush, R. I., et al. 2012, Sol. Phys., 275, 207
Staehli, M., & Magun, A. 1986, Sol. Phys., 104, 117
Tan, B. 2013, ApJ, 773, 165
Tan, B., Yan, Y., Tan, C., & Liu, Y. 2007, ApJ, 671, 964
Tan, B., Yu, Z., Huang, J., et al. 2016, ApJ, 833, 206
Tan, B., Zhang, Y., Tan, C., & Liu, Y. 2010, ApJ, 723, 25
Tan, C., Yan, Y., Tan, B., et al. 2015, ApJ, 808, 61
Tan, C., Yan, Y., Tan, B., & Xu, G. 2009, Science in China: Physics, Mechanics and Astronomy, 52, 1760
Tingay, S. J., Oberoi, D., Cairns, I., et al. 2013, in Journal of Physics Conference Series, 440, 012033
van Haarlem, M. P., Wise, M. W., Gunst, A. W., et al. 2013, A&A, 556, A2
Wang, F., Mei, Y., Deng, H., et al. 2015, PASP, 127, 383
Wang, W., Yan, Y., Liu, D., et al. 2013, PASJ, 65, S18
Willson, R. F., Lang, K. R., & Liggett, M. 1990, ApJ, 350, 856
Xie, R. X., Song, Q., Wang, M., & Chen, G. Q. 1994, Sol. Phys., 155, 113
Xie, R.-x., & Wang, M. 2000, Chinese Astronomy and Astrophysics, 24, 241
Yan, Y., Chen, L., & Yu, S. 2016, in Solar and Stellar Flares and their Effects on Planets, eds. A. G. Kosovichev, S. L. Hawley, & P. Heinzel, 320, 427
Yan, Y., Tan, C., Xu, L., et al. 2002, Science in China A: Mathematics, 45, 89
Yan, Y., Chen, Z., Wang, W., et al. 2021, Frontiers in Astronomy and Space Sciences, 8, 20
Yu, S., & Chen, B. 2019, ApJ, 872, 71
Yu, S., Chen, B., Reeves, K. K., et al. 2020, ApJ, 900, 17
Zhang, Y., Tan, B., Karlický, M., et al. 2015, ApJ, 799, 30